Supplementary Materials

Dynamic stability of active sites in hydr(oxy)oxides for the oxygen evolution reaction

Dong Young Chung[1], Pietro P. Lopes[1], Pedro Farinazzo Bergamo Dias Martins[1], Haiying He[2], Tomoya Kawaguchi[1], Peter Zapol[1], Hoydoo You[1], Dusan Tripkovic[3], Dusan Strmcnik[1], Yisi Zhu[1], Soenke Seifert[4], Sungsik Lee[4], Vojislav R. Stamenkovic[1], Nenad M. Markovic[1]*

Correspondence to: nmmarkovic@anl.gov

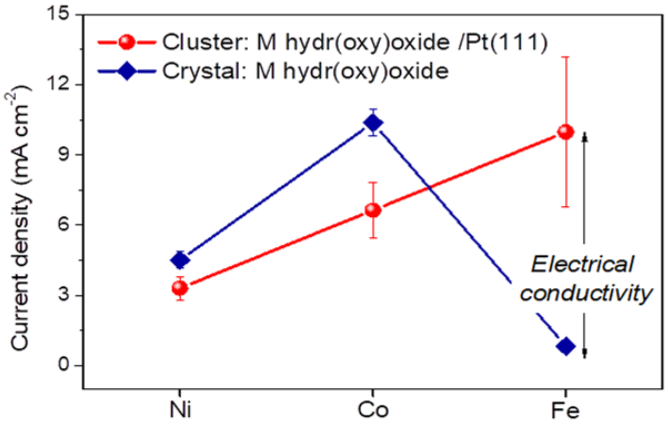

Supplementary Figure 1 OER Activity (current density at 1.7 V) trend of M hydr(oxy)oxide samples prepared by cluster on Pt(111). Electrochemical OER activity difference between cluster (M hydr(oxy)oxide/Pt(111)) and M hydr(oxy)oxide crystal derived by bulk metal crystal can be originated from the electrical conductivity of M hydr(oxy)oxide. Based on previous reports[1,2], the activity of thick and thin M hydr(oxy)oxide shows significant difference in Fe system due to low electrical conductivity compared to other systems and conductivity issue can affect overall electrochemical performance[3-5]. To compensate electrical conductivity issues, mono-layer level of hydr(oxy)oxide on Pt(111) samples were used in this study.

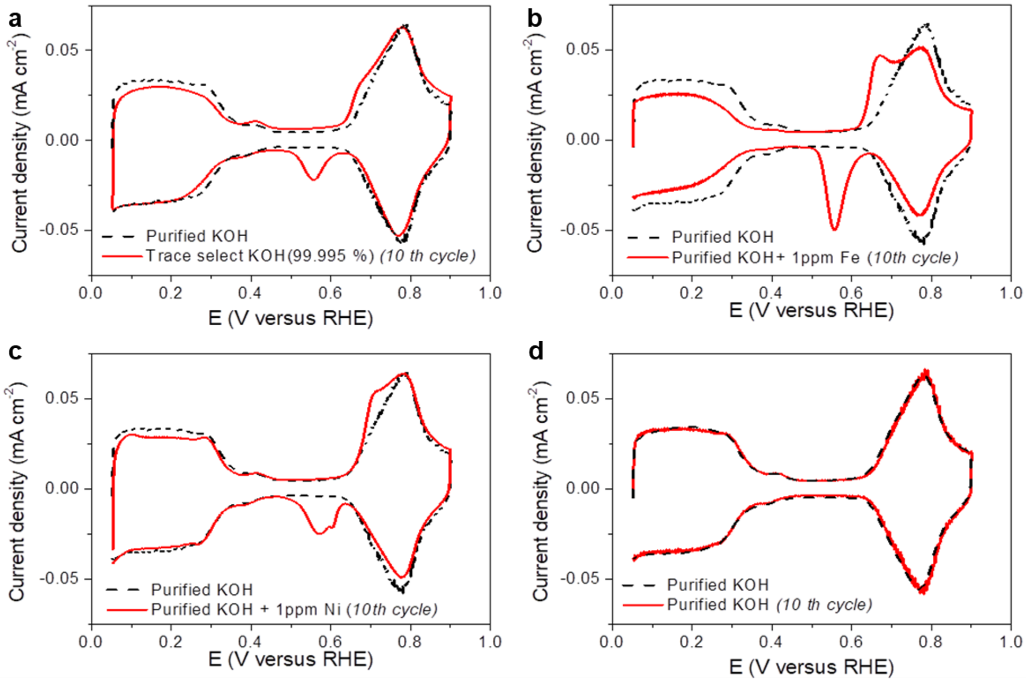

Supplementary Fig. 2 Cyclic voltammetry of Pt (111) single crystal electrode after 10 potential sweep from 0.05 to 0.9 V with rotating speed of 1600 rpm in 0.1 M KOH. To compare the result, 1st cycle of CV in purified KOH by our method was presented together as black dash line. (a) Trace select level (99.995 %) of commercial KOH, (b) Purified KOH + 1 ppm of Fe(NO)$_3$, (c) Purified KOH by + 1 ppm of Ni(NO)$_3$. (d) Purified KOH.

Supplementary Note 1

Electrolyte purification and its confirmation

The major change can be summarized as three points. First, the H_{upd} is suppressed ($0.05 < E < 0.4$). Second, OH_{ad} formation starts at negative potential compared to bare Pt(111). Third, initial OH_{ad} peak becomes irreversible. Based on these features by cation effect on Pt(111) in alkaline media, we conducted electrochemical cyclic voltammograms (CV) using commercial KOH, purified and control group with specific cation dissolved in KOH electrolyte. To monitor cation effect significantly, we conducted 10 potential cycles with rotating speed of 1600 rpm. To compare electrolyte cleanness, we compare CV data (after 10 potential cycle; solid line in supplementary Figure 2) with CV which was measured in purified electrolyte (dash line in supplementary Figure 2). As shown in supplementary Figure 2a, the highest purity commercial KOH CV significantly. Given control experiment with certain cation (Fe and Ni) in purified electrolyte, Fe in commercial KOH affects electrochemical performance. While our electrochemical method shows negligible change, indicating that our method can successfully eliminate impurity which can affect electrochemical performance (supplementary Figure 2d).

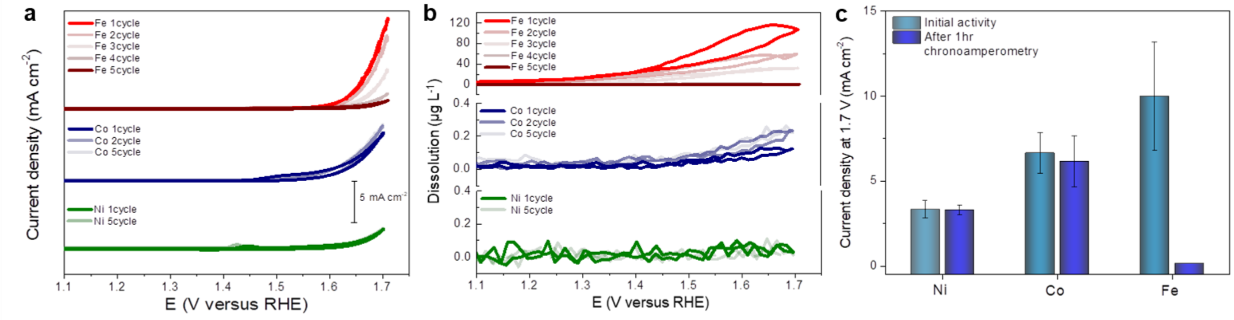

Supplementary Figure 3 Activity and stability results of M hydr(oxy)oxide in purified KOH. (a) OER activity and (b) in situ monitoring of simultaneous metal dissolution (Fe, Co and Ni) (c) chronoamperometry (at 1.7V, 1hr) results of M hydr(oxy)oxide. OER activity measurement conjunction with in situ monitoring of metal dissolution by ICP-MS was conducted 5 cycles. In Fe hydr(oxy)oxide, the activity continuously decreased and the amount of Fe dissolution showed similar trend with activity decay. At 5th cycles, Fe hydr(oxy)oxide does not show apparent activity and dissolution, indicating that almost all of Fe was dissolved during 5 cycles. However, Co and Ni hydr(oxy)oxide showed good activity retention and the amount of metal dissolution is much less compared to Fe. The OER stability measurement was also conducted constant voltage method (chronoamperometry at 1.7 V, 1hr). After 1hr measurement, Ni and Co hydr(oxy)oxide showed similar current compared to initial values without appreciable activity loss, while Fe hydr(oxy)oxide showed abrupt activity loss, indicating that Fe hydr(oxy)oxide is really unstable during OER, which is same trend of continuous activity and ICP-MS measurement in Figure 1.

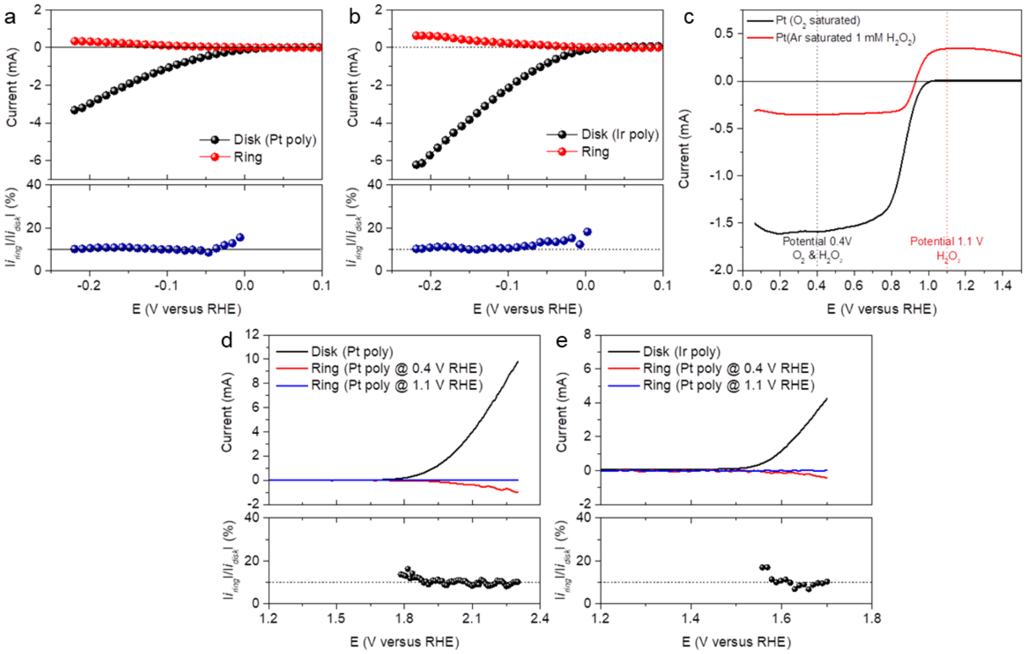

Supplementary Figure 4 RRDE method to quantify O_2 production and discussion for Faradaic efficiency of O_2 (FE_{Oxygen}). Collection efficiency calibration using HER with polycrystalline (a) Pt and (b) Ir disk, (c) cyclic voltammograms in O_2 saturated 0.1 M KOH (black) and 1 mM H_2O_2 containing 0.1 M KOH (Ar saturated, red) using Pt electrode, RRDE results for FE_{Oxygen} using polycrystalline (a) Pt and (b) Ir disk in OER region (The Ring potential was held at 0.4 and 1.1 V (versus RHE) to monitor O_2 and H_2O_2 production, respectively.).

Supplementary Note 2

The Faraday efficiency of OER (FE_{Oxygen}) using RRDE

To quantify actual production of O_2 and calculate Faradaic efficiency of O_2 (FE_{Oxygen}), we conducted rotating ring disk electrode (RRDE) method.[6-8] For calibration of collection efficiency in gas evolving reaction, we choose hydrogen evolution reaction (HER) as calibration reference since HER in Pt and Ir only produces H_2 and it is a 2 electron process without any other convoluting reactions (supplementary Figure 4a-b). To calculate collection efficiency, cyclic voltammograms were measured using Pt and Ir disk polarized into HER region while potential of ring disk (Pt) was held at 0.2 V (versus RHE), high enough potential such that HOR is under diffusional control. As shown in supplementary Figure 4a and b, current ratio ($|i_{ring}|/|i_{disk}|$, %) reaches 10%, 2.5 times lower than expected from the design and geometry of the RRDE setup (geometric collection efficiency 25%). Although this 10% collection efficiency measured experimentally is similar to the values extensively found during the O_2 monitoring from O_2 evolving catalysts[6], but its origin is unclear, because HER/HOR on Pt or Ir is a clear process, then we can assume that for a gas evolving reaction only 10% of products from the disk reaches the ring for collection. To distinguish thermodynamic possible product (H_2O_2 and O_2), we screened potential for detection of H_2O_2 (in O_2 saturated 0.1 M KOH (black) and 1 mM H_2O_2 containing 0.1 M KOH (Ar saturated, red curve in supplementary Fig. 4c) and O_2 (O_2 saturated 0.1 M KOH, black curve in supplementary Figure 4c).

H_2O_2 production (alkaline)

$$2H_2O \rightarrow H_2O_2 + 2H^+ + 2e^- \quad (E = 1.76\ V)$$

or

$$2OH- \rightarrow H_2O_2 + 2e^- \ (E = 1.76\ V)$$

O_2 production (alkaline)

$$2H_2O \rightarrow O_2 + 4H^+ + 4e^- \ (E = 1.23\ V)$$

or

$$4OH- \rightarrow 2O_2 + 4H^+ + 4e^- \ (E = 1.23\ V)$$

As shown in supplementary Figure 4c, O_2 generation is monitored using ring potential at 0.4 V (versus RHE) in diffusion limiting region (Note: we choose 0.4 V to avoid H_{upd} region for $2e^-$ O_2 reduction in Pt). For H_2O_2, we choose 1.1 V which is high enough potential for oxidizing H_2O_2 (diffusion limiting region) while below thermodynamic potential of O_2 evolution. For calculation of Faradaic efficiency of O_2, we measured 2 times with different ring potential (for H_2O_2; 1.1 V and for O_2; 0.4 V). To confirm our set-up, we tested polycrystalline Pt and Ir (supplementary Figure 4d and 4e). There is no H_2O_2 production (blue, 1.1 V) in both cases, which is related to significant high overpotential (1.78 V) than O_2 production (1.23 V). The current ratio [O_2 reduction current (ring)/OER current (disk)] reaches 10 %, indicating Pt and Ir undergo almost 100 % FE_{Oxygen} process.

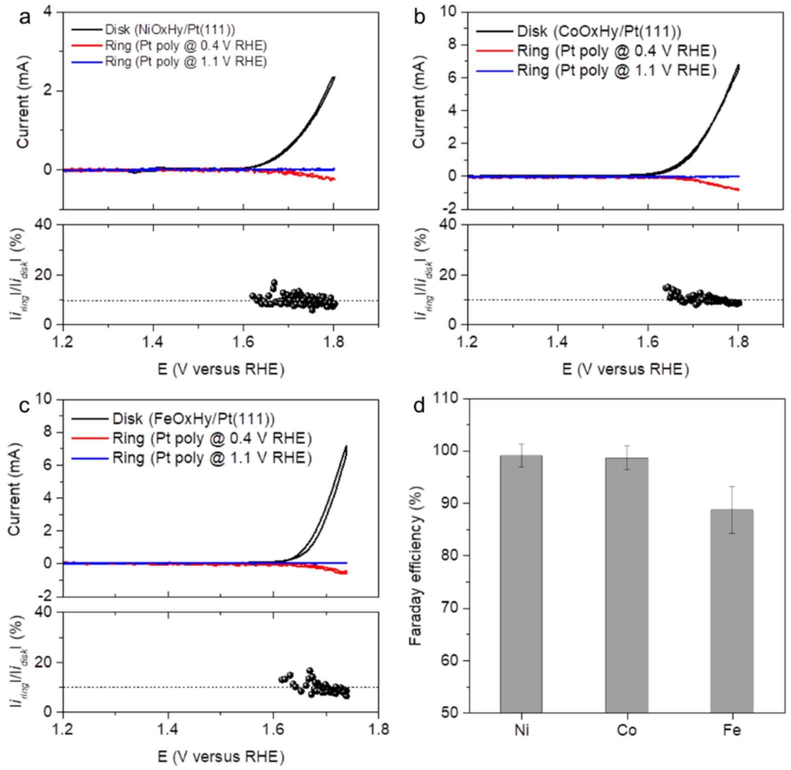

Supplementary Figure 5 RRDE measurement for Faradaic efficiency of O_2 (FE_{Oxygen}) using (a) NiOxHy, (b) CoOxHy and (c) FeOxHy (The ring potential was held at 0.4 and 1.1 V (versus RHE) to monitor O_2 production (red) and H_2O_2 production (blue), respectively. (d) Summary of Faradaic efficiency of O_2 (FE_{Oxygen}) in monometallic hydr(oxy)oxide. To quantify FE_{Oxygen}, we conducted RRDE method in monometallic hydr(oxy)oxides. As shown in supplementary Figure 5a-c, there is no H_2O_2 currents (ring polarized at 1.1V) which is due to high thermodynamic potential of H_2O_2 (1.78 V) than O_2 (1.23 V). For O_2, Ni and Co shows almost 100 %, while Fe shows around 88 % due to the significant Fe dissolution during OER measurements (supplementary Figure 5d). Taking together both FE_{oxygen} and ASF values, with absence of any H_2O_2 production, they represent the degree of material dissolution relative to O_2 production rates. In other words, they provide a quantitative basis to assess stability of materials during OER. But since ASF is determined based on direct monitoring of the dissolution rates, it is a better metric than Faradaic efficiency to evaluate simultaneously the activity and stability of technological relevant materials for OER.

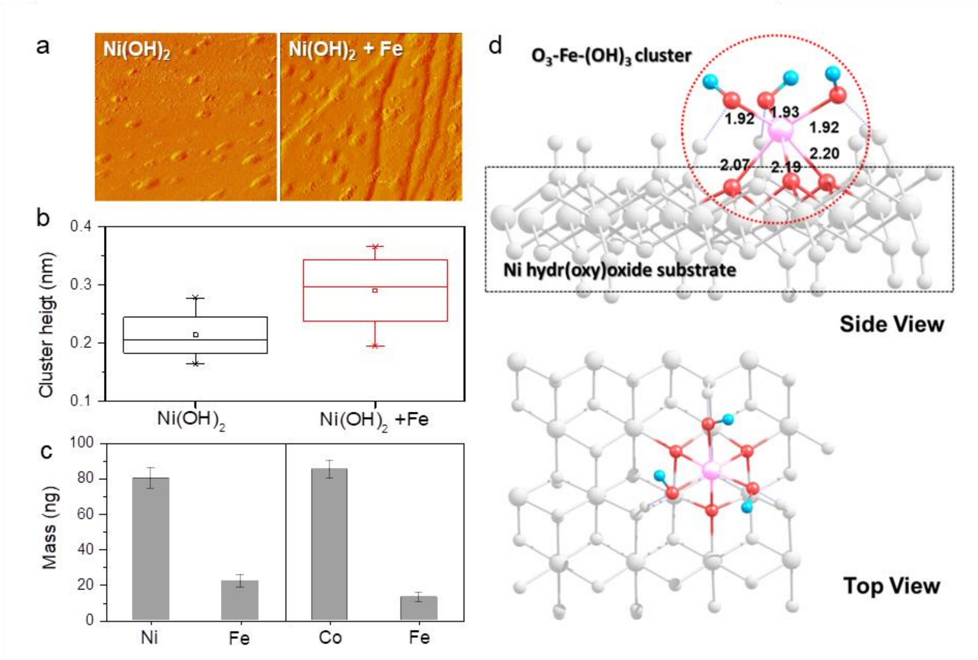

Supplementary Figure 6 (a) STM image (100 nm x 100 nm) of Ni hydr(oxy)oxide/Pt(111) and hydr(oxy)oxide/Pt(111) after Fe adsorption (b) Height of cluster. (c) ICP-MS results after Fe incorporation. (d) Geometries of adsorbed O_3-Fe$(OH)_3$ from DFT calculations. STM analysis was conducted to estimate morphology change after Fe incorporation. There is no significant change of morphology was observed, however the cluster height increases after Fe incorporation (supplementary Figure 6a). Considering height increase (supplementary Figure 6b), Fe was incorporated on Ni hydr(oxy)oxide less than 1 monolayer. Through ICP-MS analysis, the composition ratio between Ni (Co) and Fe was estimated (supplementary Figure 6c). The surface coverage of Fe on Ni and Co hydr(oxy)oxide is about 25 and 15 %, respectively. This relatively high coverage suggests that Fe species cannot be solely at the edge and defect sites, but have to involve the basal plane of MOOH. DFT calculations show that optimized geometries of Fe hydr(oxy)oxide species adsorbed on Ni hydr(oxy)oxide (supplementary Figure 6d) increase heights by less than one monolayer. This is consistent with our STM results, although detailed atomic geometry cannot be compared.

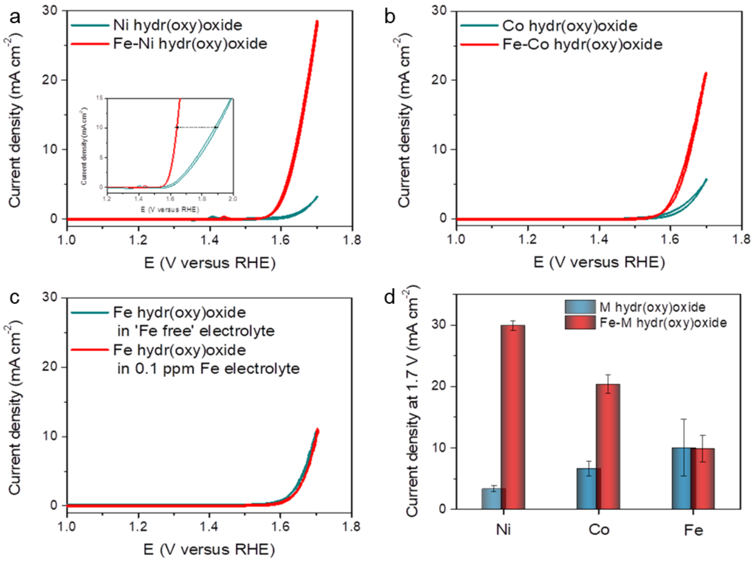

Supplementary Figure 7 First scans of OER activity of (a) Ni and Fe-Ni hydr(oxy)oxide (inset shows the overpotential to reach 10 mA cm^{-2}), (b) Co and Fe-Co hydr(oxy)oxide (c) Fe hydr(oxy)oxide in ‘Fe free’ electrolyte and 0.1 ppm of Fe containing electrolyte. (d) Summary of activity Fe-M and M hydr(oxy)oxide.

Supplementary Note 3

Fe effect on M hydr(oxy)oxide and activity comparison with previous reference

Fe-Ni and Fe-Co hydr(oxy)oxide were prepared by immersing electrolyte with 0.1 ppm of Fe in purified electrolyte. Fe incorporated samples (Fe-M hydr(oxy)oxide) showed opposite OER activity trend compared to monometallic hydr(oxy)oxide. It is hard to directly compare the turnover frequency (TOF) and overpotential to reach certain current with other papers because those values are not intrinsic. Because overpotential is highly affected by the mass loading of samples and TOF is also affected by potential[10] and the substrate[10,11] etc. Therefore, we compare the overpotential difference between Ni and Fe-Ni. Based on supplementary Table 1, the overpotential difference is comparable to previous reports.

Supplementary Table 1 Overpotential comparison for Ni and Fe-Ni hydr(oxy)oxide

Reference	Ni: overpotential (mV) to reach current density (mA cm^{-2})	Fe-Ni: overpotential (mV) to reach current density (mA cm^{-2})	Overpotential difference (mV)
Our data	666 (10 mA cm^{-2}) 470 (2 mA cm^{-2})	416 (10 mA cm^{-2}) 366 (2 mA cm^{-2})	250 104
9	371 (8 mA cm^{-2})	274 (8 mA cm^{-2})	91
10	~455 (2 mA cm^{-2})	~280 (2 mA cm^{-2})	~175
11	~420 (10 mA cm^{-2})	~300 (10 mA cm^{-2})	~125
12	529~605 (10 mA cm^{-2})	280~330 (10 mA cm^{-2})	200~320

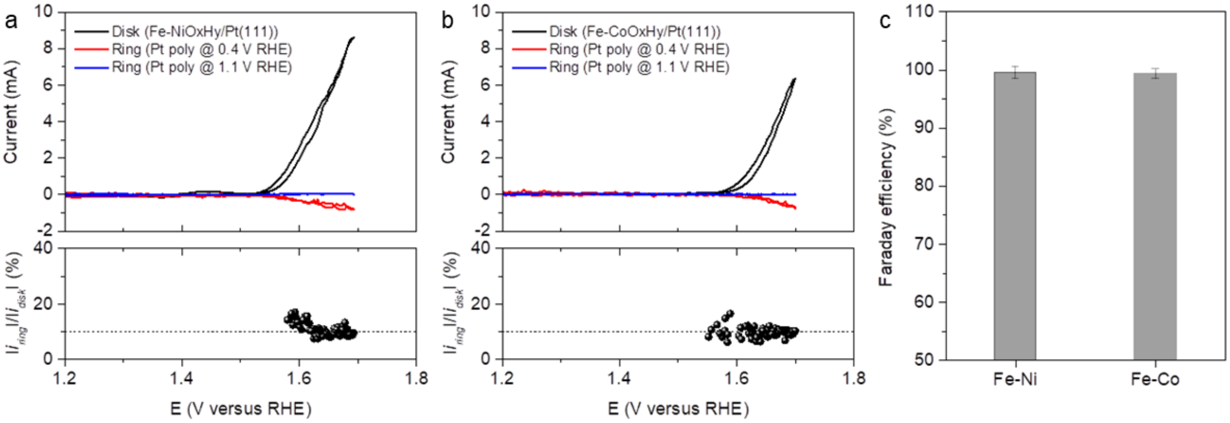

Supplementary Figure 8 RRDE measurement for Faradaic efficiency of O_2 (FE_{Oxygen}) using (a) Fe-NiOxHy and (b) Fe-CoOxHy (The ring potential was held at 0.4 and 1.1 V (versus RHE) to monitor O_2 production (red) and H_2O_2 production (blue), respectively (To avoid Fe contamination on Pt ring electrode, we measured and showed 1st cycle result using fresh electrode in purified KOH.) (c) Summary of Faradaic efficiency of O_2 (FE_{Oxygen}) in Fe-M hydr(oxy)oxide. Faradaic efficiency of O_2 (FE_{Oxygen}) reaches almost 100 % for both Fe-Ni and Fe-Co.

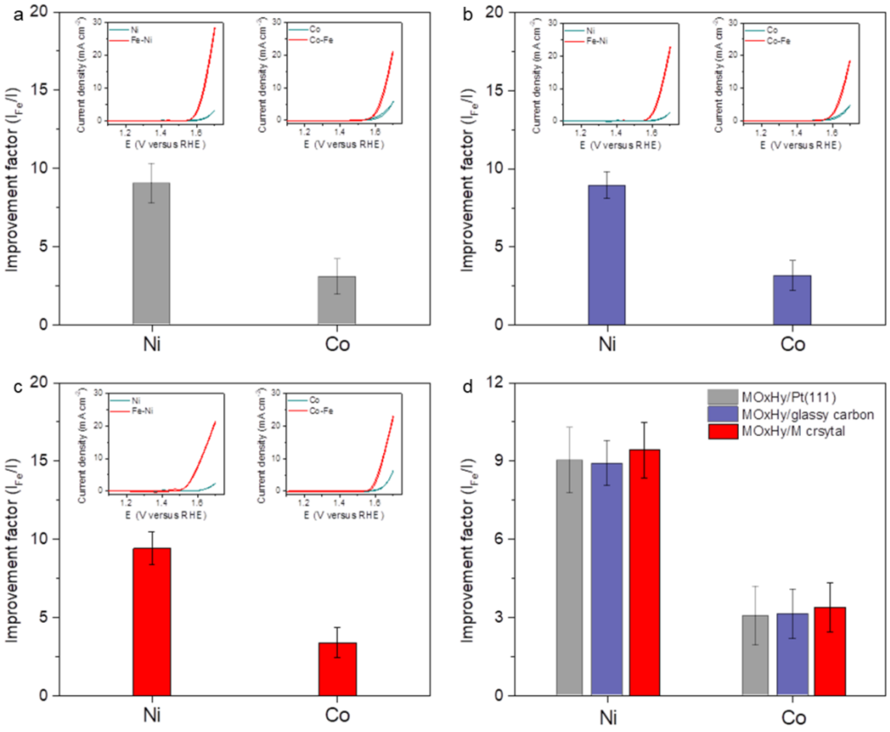

Supplementary Figure 9 OER activity (Improvement factor: I_{Fe}/I) of MOxHy (M: Ni and Co) with and without Fe (inset shows current versus potential plot) (a) MOxHy/Pt(111) (b) MOxHy/glassy carbon (c) MOxHy/M crystal, (d) summary of improvement factor (I_{Fe}/I) to discuss support effect.[13-15] Fe-M reaction is observed regardless of support, indicating that this phenomena is originated from the M hydr(oxy)oxide to Fe interface.

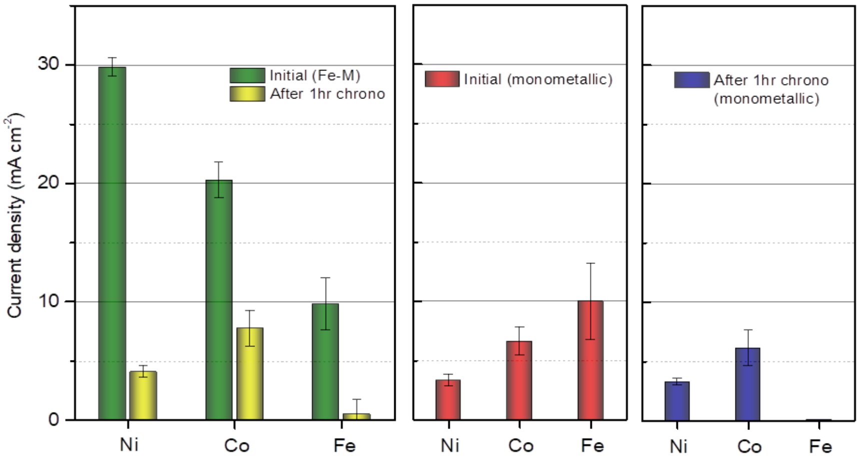

Supplementary Figure 10 Activity-stability results of Fe-M and monometallic hydr(oxy)oxide by 1hr chronoamperometry under ‘Fe free’ purified 0.1 M KOH. In purified KOH solutions, the activity of Fe-Ni and Fe-Co samples shows a remarkable deactivation after 1 hour of potential hold (1.7 V), bringing the initial high activities down to almost the same levels as monometallic hydr(oxy)oxides.

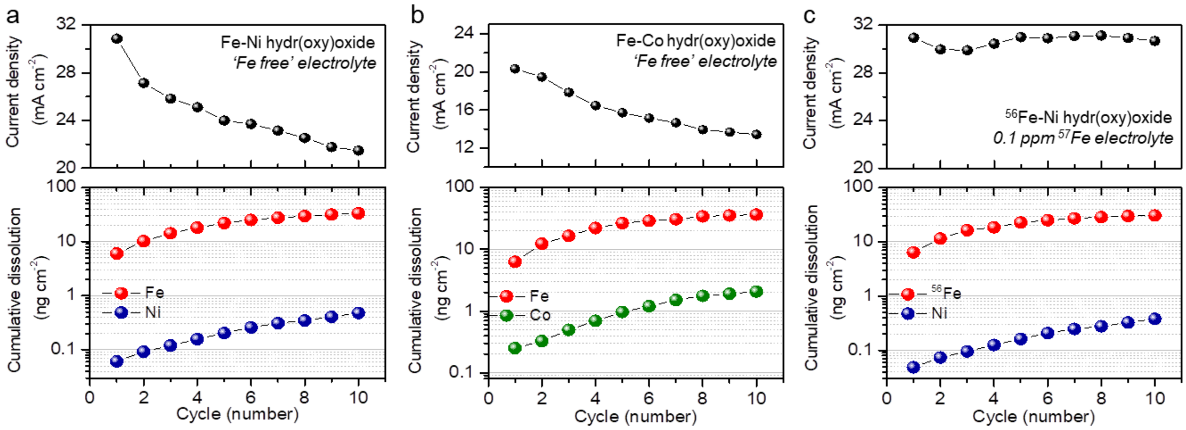

Supplementary Figure 11 Activity and stability measurement of Fe-M hydr(oxy)oxide in (a,b) 'Fe free' electrolyte and (c) 0.1 ppm of ^{57}Fe containing electrolyte OER activity and in situ monitoring of simultaneous elemental dissolution. (a) Fe-Ni hydr(oxy)oxide (b) Fe-Co hydr(oxy)oxide (c) ^{56}Fe-Ni hydr(oxy)oxide in 0.1 ppm of ^{57}Fe electrolyte. The electrochemical activity conjunction with in situ ICP-MS was conducted using Fe-Ni and Fe-Co hydr(oxy)oxide in 'Fe free' purified KOH electrolyte (supplementary Figure 11a-b). Both Fe-Ni and Fe-Co hydr(oxy)oxides show continuous activity drop with potential cycles. By monitoring elemental dissolution, Ni and Co shows stable compared to Fe while significant Fe dissolution was observed. This dissolution trend (Fe>> Co > Ni) is identical to the monometallic hydr(oxy)oxide trend (Figure 1 in manuscript and supplementary Figure 3), indicating that Fe is unstable regardless of being existed either M or Fe-M hydr(oxy)oxide. To reveal the origin of stability difference depending on existence of Fe in electrolyte, we conducted ICP-MS results under 0.1 ppm of Fe in KOH. To discern dissolution of ^{56}Fe from electrode, ^{57}Fe was used in electrolyte. As shown in supplementary Figure 11c, ^{56}Fe (from electrode) dissolution still occurs despite absence of OER deactivation after multiple cycles, strongly implying that a dynamic Fe exchange, dissolution from electrode (^{56}Fe) and deposition from electrolyte (^{57}Fe) is occurring at the interface.

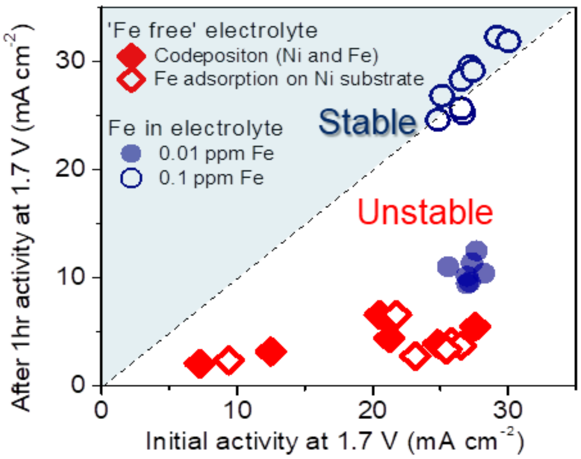

Supplementary Figure 12 Activity and stability (after 1 hr chronoamperometry at 1.7 V) summary of Fe-Ni hydr(oxy)oxide samples in ‘Fe free’ electrolyte and Fe containing electrolyte. ‘Co-deposition’ samples were prepared by potential cycling between H_{upd} and OH_{ad} region with 1-100 ppm (depending on composition ratio) of precursors ($Fe(NO)_3$ hexahydrate and $Ni(NO)_3$ hexahydrate) on Pt(111) as substrate. ‘Fe adsorption on Ni substrate’ samples were prepared by deposition of Ni hydr(oxy)oxide on Pt (111) first. Fe was incorporated in Ni hydr(oxy)oxide by $Fe(NO)_3$ spike in ‘Fe purified’ KOH electrolyte. Below certain equilibrium level of Fe in electrolyte (in our case 0.1 ppm), Fe-Ni hydr(oxy)oxides are unstable during OER.

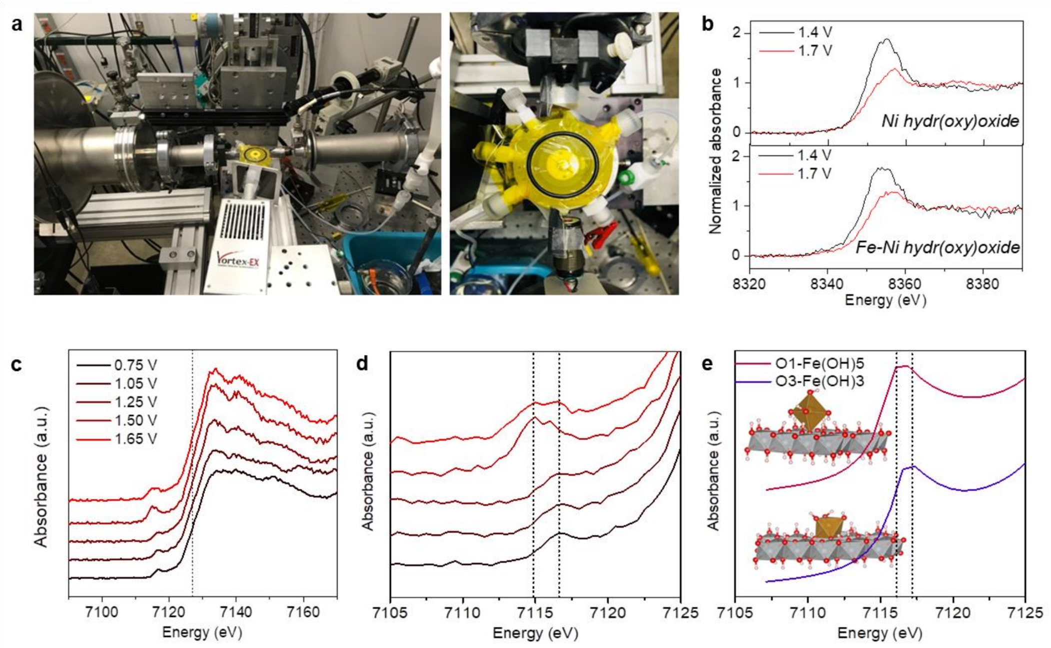

Supplementary Figure 13 (a) Digital photograph images of experimental set-up for *in-situ* XANES with grazing-incidence fluorescence mode. In situ XANES results (b) Ni K-edge of Ni hydr(oxy)oxide (up) and Fe-Ni hydr(oxy)oxide (down), (c) Fe K-edge of Fe-Ni hydr(oxy)oxide (d) Fe pre-edge region and (e) XANES pre-edge simulation results using DFT-optimized geometries (Insets show Fe geometries from DFT used for XANES simulations).

Supplementary Note 4

In situ XANES results and discussion for active site

In Ni K-edge (supplementary Figure 13b), the oxidation state change from Ni^{2+} to Ni^{3+} was observed in high potential range (1.7 V), which is related to structural change from Ni hydroxide ($Ni(OH)_2$) to Ni oxyhydroxide (NiOOH) as observed on both monometallic and bimetallic systems. However, Ni K-edge absorption spectra does not show any difference with and without Fe (supplementary Figure 13b), indicating that electronic or geometric structure change of Ni cannot be the source of higher activity when Fe is present. In the Fe K-edge region (XANES spectra in supplementary Figure 13c), changes in Fe oxidation state are not observed in the potential window from 0.75 to 1.65 V versus RHE [16], although the absence of changes does not preclude Fe participation as an active site. If a high-valent Fe (Fe >3+) species are being formed as part of the OER mechanism, the formation of high oxidation state Fe species would act as a strong oxidizing agent to produce O_2 from OH^-/H_2O. During this redox process, after removing electrons from O^{2-} centers present in OH^- or H_2O, the Fe would return to its original 3+ state. Therefore, one would expect to observe both 3+ and 4+/5+ Fe species to a varying degree. This scenario would be equivalent to OER on Ir-based catalysts in acid media, where both high-valent (5+) and reduced Ir (3+) have been observed simultaneously at OER potentials [17]. But rather than being the norm, this is just one particular condition in a balance between the kinetics of Fe oxidation by the electrode and the kinetics of OH^-/H_2O oxidation by a highly oxidized Fe species. If the reaction between $Fe^{(4+/5+)}$ and OH^-/H_2O is ultra-fast, only trace amounts of $Fe^{(4+/5+)}$ would be required as they are rapid consumed as soon as formed, making only Fe^{3+} the detectable species. On the other hand, if the kinetics of $Fe^{(4+/5+)}$ and OH^-/H_2O exchange in slow, then only small amounts of $Fe^{(3+)}$ would be measured. Both extremes still require some Fe species, and therefore, it is not necessary to accumulate large amounts of a reaction intermediate (Fe4+/5+ species in this case) in order for it to be effective as an active site. In fact, while a great majority of studies use in situ XANES to identify changes in Fe oxidation state, high oxidation state Fe (> 3+) species are rarely observed because the unoccupied Fe band can be overlapped with oxygen when Fe exists as 4+ oxidation state[18]. This electron overlap with oxygen sites is the precondition by which discharge of oxygen atoms can occur with eventual release of O_2 molecules. We note, however, that other spectroscopy methods using Mossbauer effect have shown the formation of a Fe 4+ species during OER process [19], while its role in the OER electrocatalysis was not conclusive. Additionally, only in organic electrolytes it was possible to detect such highly oxidized Fe species [20].

While there is no edge position change, significant change is observed in pre-edge region at potential above 1.5 V where Fe start to dissolve and OER occurs (supplementary Figure 13d). According to the peak position and intensity changes (shift to lower energy and peak intensity increase), local coordination change from symmetric to asymmetric can occur in high potential.[21] XANES simulation using DFT-optimized geometries of Fe with different number of OH groups (supplementary Figure 13e) suggests that Fe local structure can be significantly changed in high potential (> 1.5 V) and Fe is existed as pseudo stable condition by vigorous Fe dynamic process through dissolution and adsorption. Fe local structure analysis from O3-$Fe(OH)_3$ to O1-$Fe(OH)_5$ by XANES pre-edge DFT calculation agrees well with recent in situ extended X-ray absorption fine structure (EXAFS) analysis [22]. Since pure FeOxHy is really unstable during OER potential window, we cannot preclude the synergistic effect (Fe with NiOxHy) compared with pure FeOxHy. However, Fe is the main source for activity origin of Fe-MOxHy. Furthermore, interface between Fe species and MOxHy substrate may be critical for achieving high levels of oxygen production.

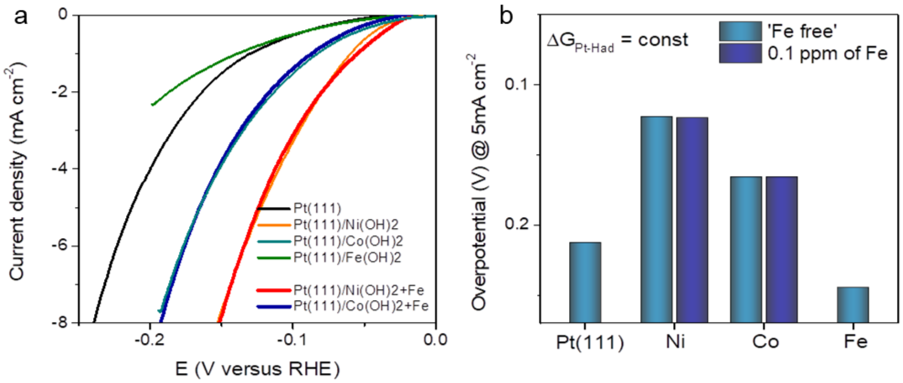

Supplementary Fig. 14 (a) HER activity of M hydr(oxy)oxide/Pt(111) in 0.1 M KOH with and without 0.1 ppm of Fe in electrolyte (b) summary of HER results.

Supplementary Note 5

HER activity trend and discussion for active site

Given the hydrogen evolution reaction (HER) activity in alkaline media of M hydr(oxy)oxide/Pt is pseudo mono-functional relation with M-OH_{ad}, the HER activity of M hydr(oxy)oxide/Pt(111) directly shows the trend of M-OH binding strength (ΔG_{OHad}) [23-25]. As shown in supplementary Figure 14a, the HER trend of M hydr(oxy)oxide/Pt (111) in 'Fe free' electrolyte is order of Ni > CO > Fe, which is same trend what we observed previously[23]. The activity trend can be interpreted as ΔG_{OHad} trend of transition metal. By increasing M-OH bond (Fe > Co > Ni), strongly bonded M-OH can poison the site for re-adsorption of water molecule, making it as spectator to blocking the active site. In Fe incorporated hydr(oxy)oxide, there is no HER activity difference compared to monometallic hydr(oxy) oxide (supplementary Figure 14b), indicating that Fe incorporation cannot not significantly change M-OH_{ad} interaction on Ni or Co. Based on HER result, we conjecture that OER activity enhancement of Fe-M system is not originated from the enhanced Ni (or Co) physicochemical properties by Fe but Fe on Ni(or Co) is active site for OER.

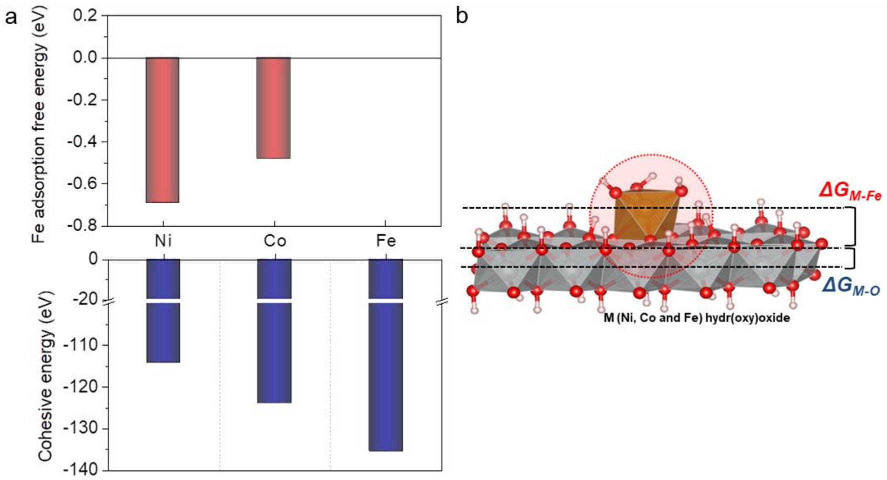

Supplementary Figure 15 (a) Average Fe adsorption free energy at 0.25 monolayer coverage (top) and cohesive energy of M (Ni, Co, Fe) hydr(oxy)oxide monolayers (bottom) calculated by DFT (b) scheme of relation between Fe adsorption energy ($\Delta G_{Fe\text{-}M}$) and cohesive energy ($\Delta G_{M\text{-}O}$). Cohesive energy of monometallic hydr(oxy)oxide monolayers was calculated based on the 2×4(001) supercell model. The reported values are for 16 MOOH units. As shown in supplementary Figure 15, the average Fe adsorption free energy ($\Delta \bar{G}_{Fe-M}$) at 0.25 monolayer coverage trend shows order (Ni < Co < Fe) which is opposite trend of cohesive energy. The latter is a metric for M-O cohesive energy ($\Delta G_{M\text{-}O}$). In calculating Fe adsorption free energy, we have used the following free energy corrections in Supplementary Table 2 and 3.

Supplementary Table 2 Contributions to the Gibbs free energy from the zero-point energy correction (ZPE), enthalpic temperature correction ($\int C_p\,\mathrm{d}T$), and entropy correction ($-TS$) for molecular species. The electronic energy in the gas phase E[gas], solvation energy, and the Gibbs free energy G are also listed. All values are given in eV.

molecules	E[gas]	Solvation Energy	ZPE	$\int C_p\,\mathrm{d}T$	$-TS$	G
H_2O	-14.22	-0.32	0.57	0.10	-0.67	-14.22
H_2	-6.76	0.01	0.27	0.09	-0.37	-6.77
$Fe(OH)_3(OH_2)_3$	-81.44	-0.98	3.00	0.45	-1.61	-80.57

Supplementary Table 3 Contributions to the Gibbs free energy from the zero-point energy correction (ZPE), enthalpic temperature correction ($\int C_p\,\mathrm{d}T$), and entropy correction ($-TS$) for bare hydroxyoxide surfaces and surfaces with Fe adsorbates. Together with the free energy corrections for the molecules (Supplementary Table 2), the total free energy correction ΔG_{corr} is calculated for the differential adsorption free energy of Fe complex on NiOOH, CoOOH and FeOOH surfaces, respectively. The electronic energy in the gas phase E[gas], in the solvated phase E[sol], and the adsorption free energy at the Fe coverage (0.25) are listed. All values are given in eV (Note that the same total free energy corrections ΔG_{corr} for the adsorption free energy of Fe complex on NiOOH, CoOOH and FeOOH surfaces calculated using one Fe complex per surface supercell have been used for higher coverages).

surfaces	E[gas]	E[sol]	ZPE	$\int C_p\,\mathrm{d}T$	$-TS$	ΔG_{corr}	$\boldsymbol{\Delta G_{\mathrm{M-Fe}}}$
NiOOH surface	-318.66	-320.73	8.02	1.57	-2.63	-	-
$Fe(OH)_3$* on NiOOH	-358.56	-360.56	9.10	1.76	-2.99	-0.94	-0.69
CoOOH surface	-349.17	-351.04	8.03	1.59	-2.70	-	-
$Fe(OH)_3$* on CoOOH	-389.07	-391.06	9.18	1.72	-2.92	-0.78	-0.48
FeOOH surface	-389.27	-392.18	7.88	1.65	-2.87	-	-
$Fe(OH)_3$* on FeOOH	-428.50	-430.66	9.00	1.79	-3.12	-0.83	0[a]

[a] Note that the adsorption of Fe complex on FeOOH does not show to be favorable and the adsorption free energy is set to zero.

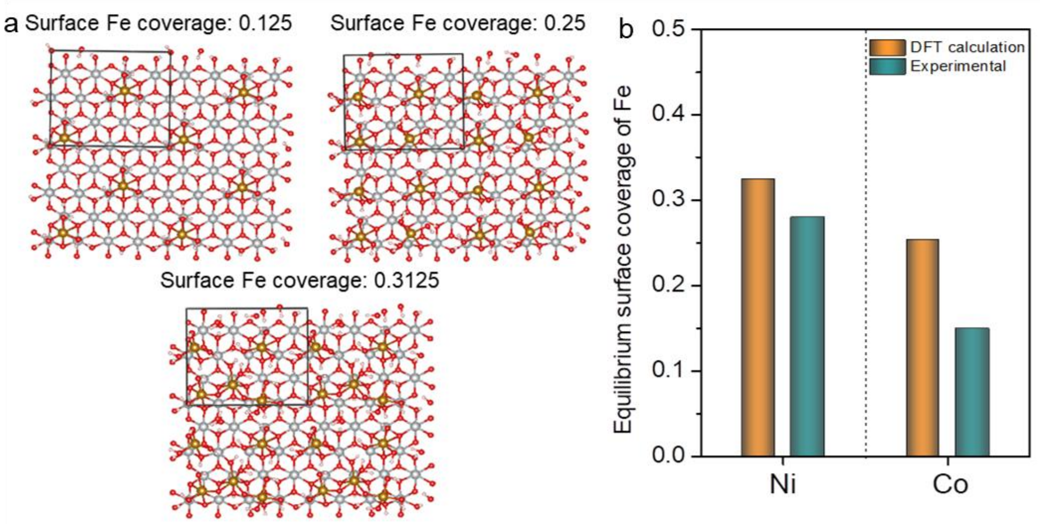

Supplementary Figure 16 (a) DFT-optimized geometries for Fe species on Ni hydr(oxy)oxide (b) Summary of maximum Fe surface coverage by experimental and computational methods. First-principles calculations were performed for Fe species on NiOOH and CoOOH surfaces with Fe coordinated by different numbers of surface oxygen and hydroxyl groups. Calculated free energies of adsorbed Fe species with different number of bonds to the surface and hydroxyl groups (supplementary Figure 6) indicate that $Fe(OH)_3$ species binding to three surface oxygen are present at potentials above 1 V versus RHE and pH=13 relevant to the OER reactions. Optimized geometries at different coverage for Fe-NiOOH are shown in supplementary figure 16a. Saturation coverage is defined as the coverage corresponding to zero differential adsorption free energy. The saturation coverage of Fe on NiOOH is higher than that of CoOOH (supplementary figure 16b), which well matches with experimental results (Fig. 3d in manuscript).

Supplementary Note 6

Estimating number of dynamically stable Fe active sites in M hydr(oxy)oxide materials (Derivation of Equations 1 and 2 in manuscript)

In general, the OER activity can be modeled by the following equation

$$i_{OER} = i^0 N \exp\left(\frac{\beta F(E - E^0)}{RT}\right) \quad (a)$$

where i_{OER} is the measured OER current density; i^0 is the exchange current density which depends on OH^- concentration and on the Gibbs energy of adsorption of reactive intermediates (ΔG_{ad}) for active site; N is the number of surface active site (dimensionless unit); β is the symmetry factor, E^0 is the equilibrium potential for OER, F is Faradaic constant, R is ideal gas constant and T indicates temperature. The number of active site (N) can be estimated by the surface area of electrocatalyst with respect to its geometric surface area and being considered a fixed value in static conditions.

To consider the vigorous surface dynamic process (dissolution and redeposition), the number of *dynamically stable active site (N^*)* should be considered instead. The derivation of the number of dynamically active site in our system; dissolution of active site (Fe) and redeposition of active species on stable substrate (M hydr(oxy)oxide) is as follows.

If we consider that Fe can interact with M hydr(oxy)oxide (MOxOHy) strongly enough to become dynamically stable at the electrode surface, even though it will be dissolving at some rate, then the incorporation reaction of Fe into M hydr(oxy)oxide can be considered similar to a surface adsorption process, with corresponding elementary reaction as:

$$Fe_{(aq)} + M_{O_xOH_y} \leftrightarrow FeM_{O_xOH_y}{}_{(ad)} \qquad (1)$$

Thus, the equation describing the equilibrium Fe content in the M hydr(oxy)oxide material can be given by:

$$q\,\frac{d\theta_{Fe}}{dt} = r_{dep} C^0_{Fe} \theta_{MO_xOH_y} - r_{diss}\theta_{Fe} \qquad \text{Eq. 1}$$

$$\theta_{MO_xOH_y} = 1 - \theta_{Fe} \qquad \text{Eq. 2}$$

Where q is the mass fraction of MO_xOH_y that can interact with Fe, and therefore determines the maximum amount of Fe that a given material can retain; given in ng.cm^{-2}. θ_{Fe} is the average fraction of Fe in the material with respect to its maximum amount at a given time *t*. θ_{MOxOHy} is the average fraction of M hydr(oxy)oxide that can interact with Fe species. r_{dep} is the overall rate of Fe deposition (takes into account both transport from electrolyte bulk to the surface and intrinsic deposition rate) while $C_{Fe}{}^0$ is the Fe concentration in the electrolyte; the overall deposition rate $r_{dep}C_{Fe}{}^0$ is given in ng.cm^{-2}.s^{-1}. r_{diss} is the Fe dissolution rate from the material; is given in ng.cm^{-2}.s^{-1}. Note that equation 2 defines that a M_{OxOHy} site that can interact with Fe is either free or occupied by Fe species. Considering that the Fe species interacting with M hydr(oxy)oxide will be the active sites for OER, the total number of Fe sites (N^*_{Fe}) is given by:

$$N^*_{Fe} = (q/q_{total})\theta_{Fe} \qquad \text{Eq. 3}$$

Thus, equation 3 defines that to increase the number of active sites for OER we need both Fe as the true active site while we need M hydr(oxy)oxide material to be a host for Fe species, holding Fe near the electrode surface long enough to be able to participate in the OER mechanism, interacting with Fe strongly to surpass the dissolution rate and establish a dynamically stable interface. By determining the values of q and θ_{Fe} we can estimate how the dynamic stability condition can be established and what factors could be tuned to enhance the overall performance.

We shall begin by establishing how θ_{Fe} depends on deposition and dissolution rates as well as on Fe content in the electrolyte. By integrating Eq. 1 and using the following boundary conditions: the equilibrium Fe fraction (${\theta_{Fe}}^{Eq}$) is reached at long times (t=∞) and the initial Fe fraction is 0 at time = 0; we arrive at:

$$\theta_{Fe} = \theta_{Fe}^{Eq}(1 - e^{-\gamma\, t}) \qquad \text{Eq. 4}$$

$$\theta_{Fe}^{Eq} = \frac{r_{dep}C_{Fe}^{0}}{r_{dep}C_{Fe}^{0} + r_{diss}} \qquad \text{Eq. 5}$$

$$\gamma = \frac{r_{dep}C_{Fe}^{0} + r_{diss}}{q} \qquad \text{Eq. 6}$$

From equations 4 through 6 we can obtain two important results: first, at steady state, the dynamic fraction of Fe is determined by a ratio function between the deposition rate and the dissolution rate, and the overall deposition rate is proportional to Fe concentration in the electrolyte; and second, although an increase in the electrolyte Fe concentration increases the deposition rate, the amount of Fe in the oxyhydroxide host will eventually saturate at sufficiently high Fe concentration in the electrolyte.

To support our model and unravel deposition kinetics, we conducted Fe spike experiment during chronoamperometry measurement using Ni hydr(oxy)oxide in supplementary Figure 17).

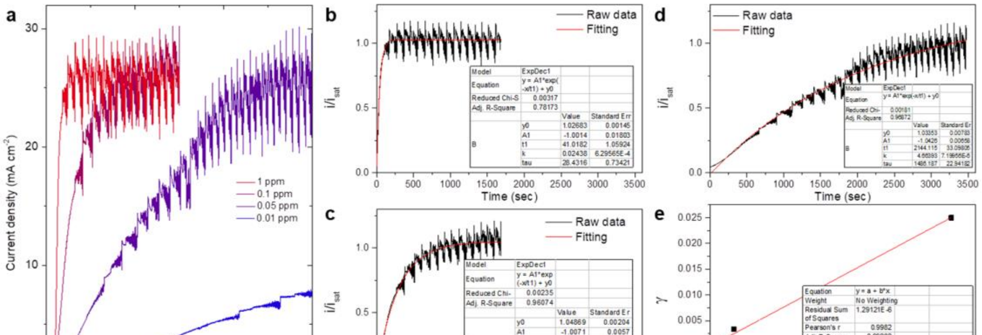

Model	ExpDec1		
Equation	y = A1*exp(-x/t1) + y0		
Reduced Chi-S	0.00317		
Adj. R-Square	0.78173		
		Value	Standard Err
B	y0	1.02683	0.00145
	A1	-1.0014	0.01803
	t1	41.0182	1.05924
	k	0.02438	6.29565E-4
	tau	28.4316	0.73421

Model	ExpDec1		
Equation	y = A1*exp (-x/t1) + y0		
Reduced Chi-	0.00235		
Adj. R-Square	0.96074		
		Value	Standard Er
B	y0	1.04869	0.00204
	A1	-1.0071	0.0057
	t1	291.309	3.25768
	k	0.00343	3.83883E-5
	tau	201.920	2.25805

Model	ExpDec1		
Equation	y = A1*exp(-x/t1) + y0		
Reduced Chi-	0.00181		
Adj. R-Square	0.96872		
		Value	Standard Er
B	y0	1.03353	0.00783
	A1	-1.0426	0.00658
	t1	2144.115	33.09806
	k	4.66393	7.19856E-6
	tau	1486.187	22.94182

Equation	y = a + b*x		
Weight	No Weighting		
Residual Sum of Squares	1.29121E-6		
Pearson's r	0.9982		
Adj. R-Square	0.99282		
		Value	Standard Err
?$OP:A=1	Intercept	5.20616E	8.731E-4
	Slope	0.02504	0.0015

Supplementary Figure 17 (a) OER chronoamperometry measurement (at 1.7 V) of Ni hydr(oxy)oxide. Each concentration of Fe precursors are spiked in 'Fe free' KOH at 120 sec. During chronoamperometry measurement (1.7 V) using Ni hydr(oxy)oxide in 'Fe free' electrolyte, Fe precursors were spiked in electrolyte at 120 sec. Fitting results (b) 1 ppm Fe, (c)

0.1 ppm Fe, (d) 0.05 ppm Fe and (e) result summary of γ versus C_{Fe}^{0} (Fe concentration in electrolyte)

As introducing Fe in electrolyte (120 sec), significant activity enhancement was observed. Two specific features can be summarized. First, Abrupt activity enhancement was observed in high concentration case while the current density was saturated around 27 mA cm^{-2}) in all cases except 0.01 ppm of Fe in electrolyte. Second, saturation time is dependent on the Fe concentration in electrolyte. To understand dissolution and redeposition behavior quantitatively and rationalize our model, we conducted fitting analysis using spike experiment data (supplementary Figure 17a).

Because Fe was introduced in electrolyte after 120 sec, x-axis was offset 120 and conduct fitting the results based on modification of Eq. 4 as

$$\frac{\theta_{Fe}}{\theta_{Fe}^{Eq}} = \frac{i}{i_{sat}} = (1 - e^{-\gamma\, t})$$

As shown in Fig. S13E, electrochemical results are well fitted by the following equation and shows linear relation between γ versusC_{Fe}^{0}, validating that our model can elucidate experimental results well.

Having established the expression for θ_{Fe} we proceed to determine the factor controlling the value of q. Considering that, at first, the number of M_{OxOHy} sites that can interact with Fe can vary from zero (poor interaction) to all of the surface sites being able to dynamically hold Fe at the interface (strong interaction), then we can write an expression for q that depends on a ΔG_{Fe-M}, which is the interaction energy between Fe species and the M hydr(oxy)oxide sites, and on the total amount of M hydr(oxy)oxide present at the electrode surface (q_{total}).

$$\frac{q}{q_{total} - q} = e^{\frac{-\Delta G_{Fe-M}}{RT}} \qquad \text{Eq. 7}$$

Equation 7 is a similar expression as the Lagmuir isotherm, as it limits the value of q between 0 and the maximum amount of M oxyhydroxide present at the surface (q_{total}), and the energetic term (ΔG_{Fe-M}) can accommodate both strong or weak interaction (Fe- binding energy) by assuming a more negative or a less negative to positive values, respectively. Rearranging equation 7 to isolate q leads to the following expression:

$$\frac{q}{q_{total}} = \frac{1}{1 + e^{\frac{\Delta G_{Fe-M}}{RT}}} \qquad \text{Eq. 8}$$

Therefore, combining equations 3, 5, and 8 gives us the final expression for the number of dynamic active sites of Fe in M oxyhydroxide materials. (***Equation 1 in manuscript***)

$$N_{Fe}^{*} = \left(\frac{1}{1 + e^{\frac{\Delta G_{Fe-M}}{RT}}}\right)\left(\frac{r_{dep} C_{Fe}^{0}}{r_{dep} C_{Fe}^{0} + r_{diss}}\right) \qquad \text{Eq. 9}$$

The key takeaway from equation 9 is that in order to scale the number of dynamically stable active sites it is necessary to ensure a strong interaction between Fe and the host (more negative $\Delta G_{Fe\text{-}M}$), as well as keeping the Fe content in the electrolyte high enough (high C_{Fe}^{0}) to balance out the dissolution rate.

Using newly derived dynamically stable active site (N^*) and surface area of host materials (A), we propose OER activity can be expressed as equation Eq.10 (***Equation 2 in manuscript***)

$$i_{OER} = i^{0,*} N_{Fe}^{*} \exp\left(\frac{\beta F(E-E^0)}{RT}\right) \qquad \text{Eq.10}$$

$$i^{0,*} = i^0 q_{total} \qquad \text{Eq.11}$$

where N_{Fe}^{*} is the number of dynamically stable active site and the exchange current density $i^{0,*}$ depends on the total amount of the exposed hydr(oxy)oxide host.

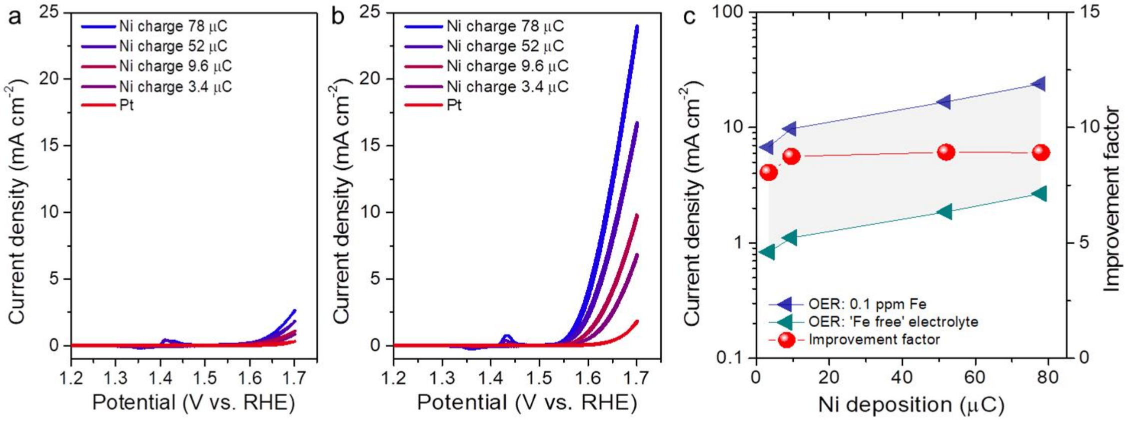

Supplementary Figure 18 Ni hydr(oxy)oxide area effect for OER activity (a) OER activity in 'Fe free' 0.1M KOH (b) in 0.1 ppm of Fe containing KOH (c) Summary of activity and activity improvement factor ($i_{OER}^{Fe}/i_{OER}^{Fe\text{-}free}$). Charge of Ni hydr(oxy)oxide films was calculated by the anodic oxidation transition peak (Ni^{2+} to Ni^{3+}) around 1.4 V. The amount of Ni hydr(oxy)oxide on Pt(111) is controlled by the Ni precursor concentration. The amount of Ni hydr(oxy)oxide is estimated pre-peak (around 1.4 V) where structure transition from $Ni(OH)_2$ to NiOOH is evolved. By increasing the amount of Ni hydr(oxy)oxide, OER activity enhanced in both 'Fe free' KOH electrolyte (supplementary Figure 18a) and 0.1 ppm of Fe in purified KOH (supplementary Figure 18b). Interestingly, the activity improvement factor ($i_{OER}^{Fe}/i_{OER}^{Fe\text{-}free}$) is identical as around 9, indicating that major activity enhancement was originated from Ni hydr(oxy)oxide-Fe interface.

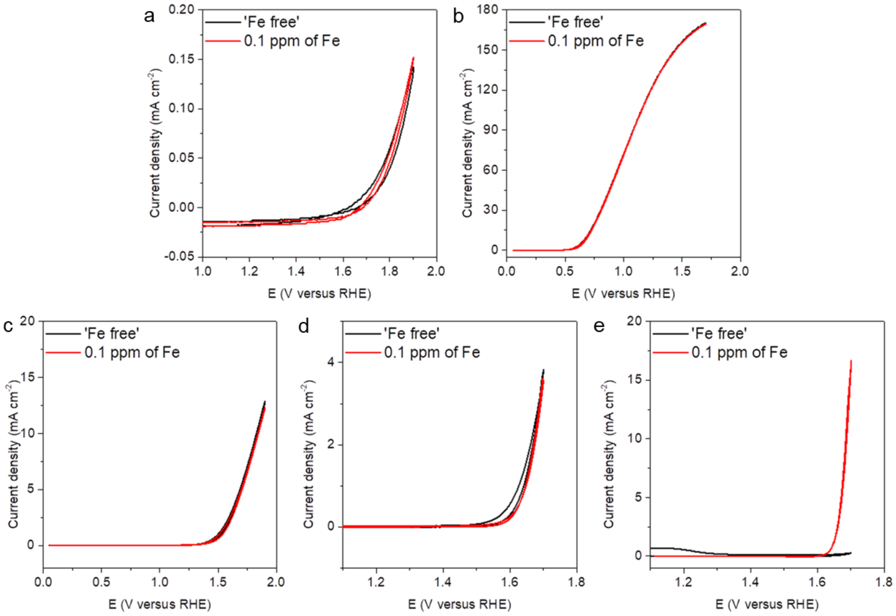

Supplementary Figure 19 Activity comparison of 3d transition metal element in ‘Fe free’ electrolyte and 0.1 ppm of Fe containing electrolyte (a) Ti, (b) V, (c) Cr, (d) Mn and (e) Cu. To find alternative materials for strong interaction with dynamic stable active Fe species in alkaline electrolysis 3d transition metal element was investigated from Ti to Cu (The data from Fe, Co and Ni is shown in supplementary Figure 5). Supplementary Figure 19 shows that there is no promotional effect with Fe in electrolyte except for Cu. Left element from the Fe shows no promotional effect with Fe, indicating that (M-O)-Fe bond (Fe adsorption) is too weak to dwell on the surface in OER region due to the strong M-O bond. This trend is well supported by the general trend that the far to the left in the periodic table, the stronger the bond. Cu shows significant high OER values when Fe is in electrolyte. The OER activity improvement factor shows over 50 which is the highest values in 3d transition metal, presenting the possibility as alternatives for current Ni based system.

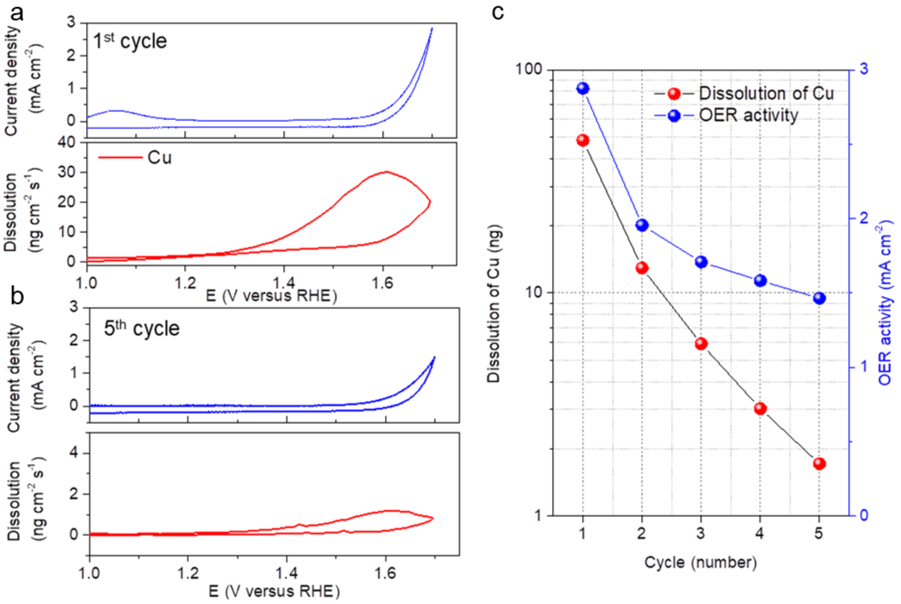

Supplementary Figure 20 In situ ICP-MS and current-potential profile results of Cu hydr(oxy)oxide/Pt(111). (a) 1st cycle (b) 5th cycle and summary results of dissolution of Cu and OER activity (at 1.7 V versus RHE). Stability for Cu hydr(oxy)oxide/Pt(111) was investigated in situ ICP-MS during cyclic voltammograms. As shown in supplementary Figure 20, severe dissolution was observed at first cycle. During 5 consecutive potential cycles, continuous dissolution of Cu and OER activity decay was observed (supplementary Figure 20) while the amount of Cu dissolution decreased, indicating that Cu is unstable in OER potential region.

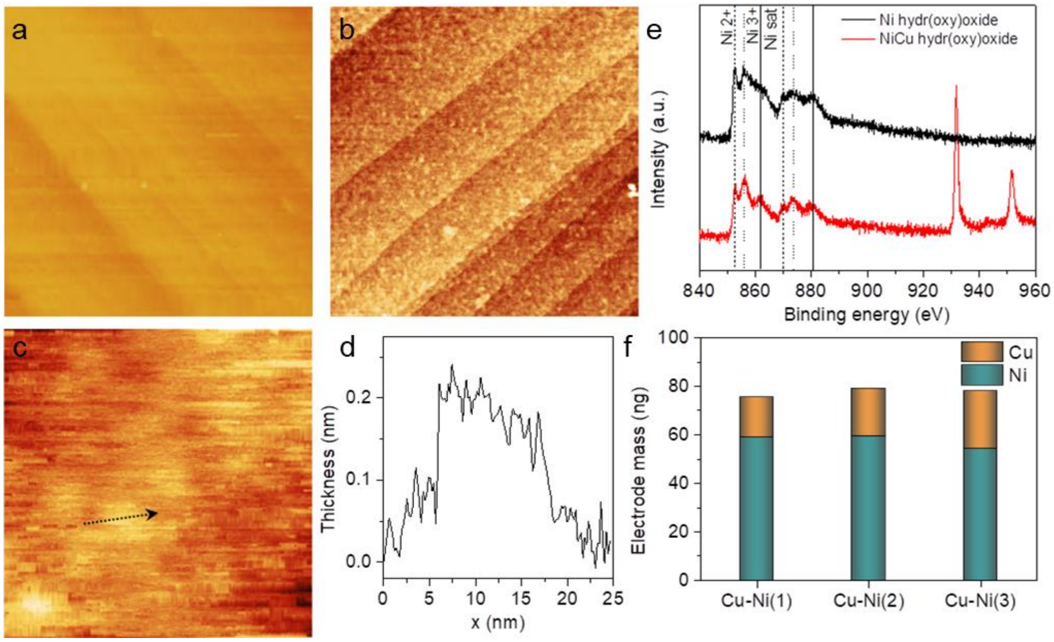

Supplementary Figure 21 Characterization of NiCu AFM images of (a) Pt (111) (b) Ni(75%)Cu (25%) hydr(oxy)oxide/Pt(111) (100 μm x 100 μm), (c) NiCu hydr(oxy)oxide (100 nm x 100 nm) arrow indicates scan for thickness measurement, (d) thickness of cluster (e) XPS analysis of Ni and NiCu hydr(oxy)oxide and (f) ICP-MS results of three independent samples to quantify Ni and Cu ratio. AFM image (supplementary Figure 21a-d) supports that NiCu hydr(oxy)oxide cluster was deposited on Pt(111) with similar morphology compared to Ni hydr(oxy)oxide (supplementary Figure 4). The height of cluster is average 0.22 nm, indicating one monolayer thickness of hydr(oxy)oxide on Pt (111). Ni 2p and Cu 2p XPS results (supplementary Figure 21e) reveal that Cu doped Ni are slightly oxidized, however both samples show 2+/3+ mixed hydr(oxy)oxide feature. The mass of NiCu was measured by ICP-MS and the mass ratio of Cu is around 25.8 % (supplementary Figure 21f) and total mass of metal hydr(oxy)oxide is similar to Ni hydr(oxy)oxide.

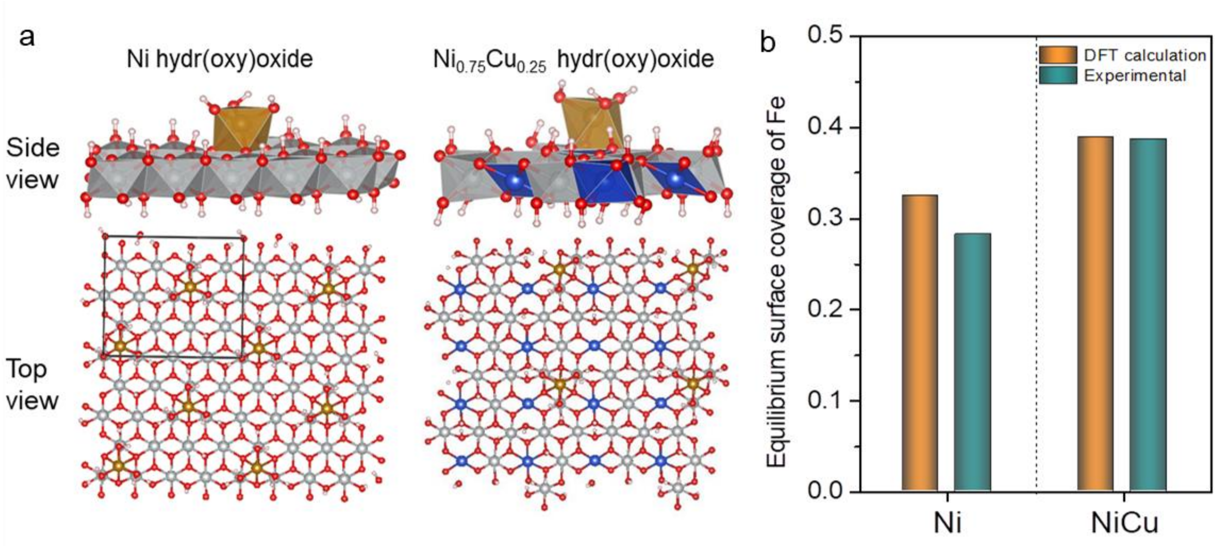

Supplementary Figure 22 (a) Side and top view of Fe-M hydr(oxy)oxide geometries from DFT used for Fe coverage calculation (b) summary of maximum Fe surface coverage by experimental (ICP-MS results) and computational method (DFT). The NiCu model was constructed by exchange 25 % of Ni with Cu based on the ICP-MS results. The saturation coverage of Fe on NiCu hydr(oxy)oxide is higher than that of Ni hydr(oxy)oxide, which supports experimental results obtained by ICP-MS. The experiments were repeated at least 3 times. The saturation coverage is defined as the coverage corresponding to zero differential adsorption free energy. For calculating Fe adsorption free energy, we have used the following free energy corrections in Supplementary Table 4.

Supplementary Table 4 Contributions to the Gibbs free energy from the zero-point energy correction (ZPE), enthalpic temperature correction ($\int C_p \, dT$), and entropy correction ($-TS$) for bare hydroxyoxide surfaces and surfaces with Fe adsorbates. Together with the free energy corrections for the molecules (Supplementary Table 2), the total free energy correction ΔG_{corr} is calculated for the differential adsorption free energy of Fe complex on NiOOH and NiCuOOH surfaces, respectively. The electronic energy in the gas phase E[gas], in the solvated phase E[sol], and the adsorption free energy at the Fe coverage (0.25) are listed. All values are given in eV. (Note that the same total free energy corrections ΔG_{corr} for the adsorption free energy of Fe complex on NiOOH and NiCuOOH surfaces calculated using one Fe complex per surface supercell have been used for higher coverages.).

surfaces	E[gas]	E[sol]	ZPE	$\int C_p \, dT$	$-TS$	ΔG_{corr}	$\boldsymbol{\Delta G_{M-Fe}}$
NiOOH surface	-318.66	-320.73	8.02	1.57	-2.63	-	-
$Fe(OH)_3$* on NiOOH	-358.56	-360.56	9.10	1.76	-2.99	-0.94	-0.69
(NiCu)OOH surface	-311.57	-313.57	8.07	1.55	-2.58	-	-
$Fe(OH)_3$* on (NiCu)OOH	-351.54	-353.59	9.18	1.73	-2.94	-0.92	-0.76

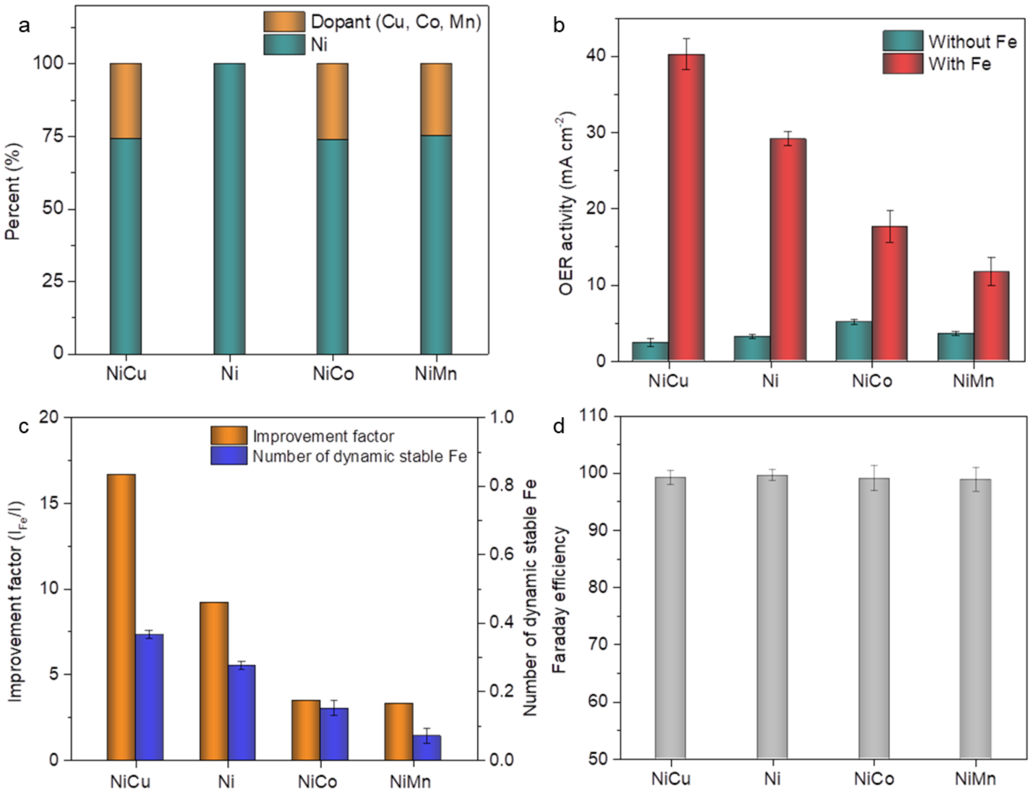

Supplementary Figure 23 (a) Elemental composition of NiM(Cu, Co, Mn) and Ni hydr(oxy)oxide samples. The composition was investigated by the ICP-MS and experiment conducted at least three times. (b) Activity trend of NiM and Ni hydr(oxy)oxide with (0.1 ppm of Fe) and without Fe in electrolyte (c) activity improvement factor (I_{Fe}/I) and following number of dynamic stable Fe (d) summary of Faradaic efficiency for O_2 production (FE_{Oxygen}) measured by RRDE method.

Supplementary Note 7

Fe effect on bimetallic (NiM) hydr(oxy)oxide substrate

OER activity trend of NiM (M: Cu, Co, Mn) and Ni hydr(oxy)oxide shows different trend with respect to existence of Fe in electrolyte. In Fe free electrolyte, the activity shows order NiCo > NiMn ≈ Ni > NiCu (supplementary Figure 23b). The OER activity trend with Fe (Fe-NiCu > Fe-Ni > Fe-NiCo > Fe-NiMn follows the activity improvement factor (I_{Fe}/I) of M (Figure 4a in manuscript, supplementary Figure 23b). By comparing the current with Fe and without Fe, we investigate the activity improvement factor of NiM samples. The NiCu shows the highest value, which is similar trend with improvement factor of M hydr(oxy)oxide. To correlate improvement factor with the number of Fe based on our model (equation 1 in our manuscript), we quantified the number of dynamic stable Fe supplementary Figure 23c). From the equation 3 in supplementary information, we calculated the values (Note, q/q_{total} is assumed 1 based on the STM and AFM analysis in supplementary Figure 6 and 21). The fraction of Fe (θ_{Fe}) was estimated by the mass balance as follows

$$\theta_{Fe} = \text{mass of Fe / [mass of host element (Ni, Cu, Co, Mn)]}$$

The potential cycle in 0.1 ppm Fe containing solution and potential hold at 1.7 V (10 min) was conducted to reach the dynamic equilibrium with dissolution and deposition. Finally the electrode was dissolved in 1 % nitric acid and quantified the mass of element through ICP-MS. The experiment was conducted at least three times in each element to get statistical meaning. All of NiM(Cu, Co, Mn) systems show high Faradaic efficiency for O_2 production (FE_{Oxygen}) around 100 %, confirming that most of current (observed in cyclic voltammograms) is originated from actual O_2 production (supplementary Figure 23d).

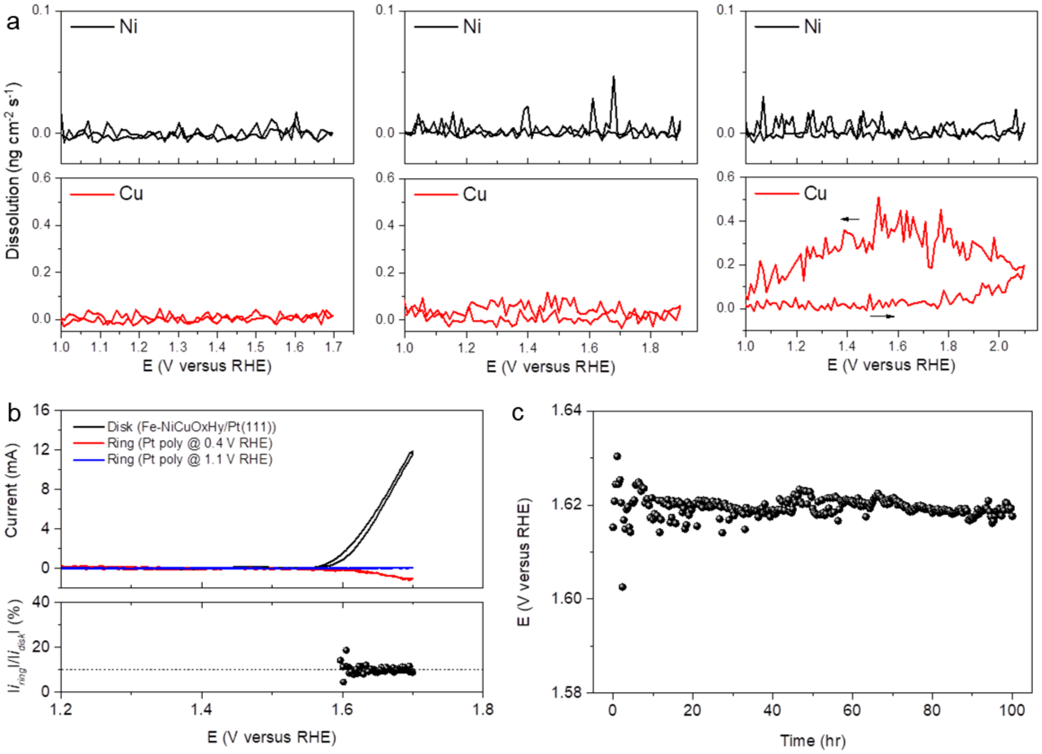

Supplementary Figure 24 (a) In situ monitoring of metal dissolution for NiCu hydr(oxy)oxide using ICP-MS potential up to 1.7 V (left), 1.9 V (middle) and 2.1 V (right) versus RHE, (b) RRDE measurement for Faradaic efficiency for O_2 production (FE_{Oxygen}) of Fe-NiCu (ring potential was held at 0.4 and 1.1 V (versus RHE) to monitor O_2 production (red) and H_2O_2 production (blue), respectively. (c) Constant current method (10 mA cm^{-2}) to monitor electrochemical stability of Fe-NiCu hydr(oxy)oxide in 0.1 ppm of Fe containing KOH. Both Ni and Cu showed stable without appreciable dissolution up to 1.9 V (supplementary Figure 24 a). When compared to pure Cu hydr(oxy)oxide (supplementary Figure 20), Ni hydr(oxy)oxide structure can stabilize Cu dopant up to certain condition (1.9 V versus RHE). RRDE results show that observed current is originated from the actual O_2 evolution (supplementary Figure 24b), which is good agreement with in situ ICP data. We also conducted long-term operation to validate stability in constant current method (10 mA cm^{-2}). Supplementary Figure 24c supports that NiCu is stable in Fe containing solution without appreciable potential change during 100 hr. Both in situ ICP-MS (material stability) and constant current method (electrochemical stability) successfully demonstrated that Fe-NiCu can be a good active site/host pair as highly active and durable candidate for OER.

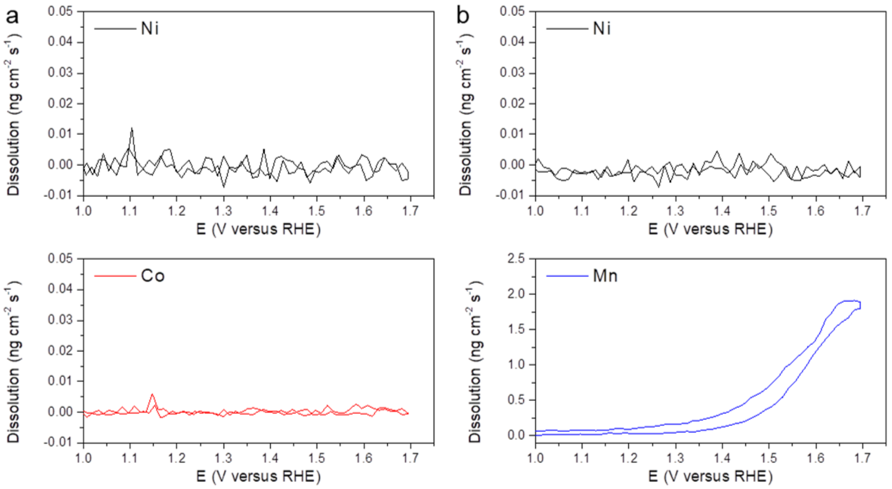

Supplementary Fig. 25 *in situ* ICP-MS results to show elemental dissolution during cyclic voltammograms (a) NiCo and (b) NiMn hydr(oxy)oxide. In situ ICP-MS results of NiCo hydr(oxy)oxide shows stable without dissolution. From the results from NiCu (supplementary Figure 24) and NiCo (supplementary Figure 25a), Ni hydr(oxy)oxide structure can stabilize M dissolution significantly. However, significant Mn dissolution is still observed in NiMn hydr(oxy)oxide(supplementary Figure 25b). Based on this observation, the ASF of Mn containing samples show low value, supporting that vulnerable to OER electrocatalyst in alkaline media. Furthermore, NiCo shows higher ASF value compared to Co due to the significant enhancement of Co stability albeit NiCo and Co shows similar OER activity. As discussed in several examples, ASF is important to consider activity and stability simultaneously.

Supplementary references

1. Burke, M. S. et al. Oxygen Evolution Reaction Electrocatalysis on Transition Metal Oxides and (Oxy)hydroxides: Activity Trends and Design Principles. *Chem. Mater.* **27**, 7549-7558 (2015).
2. Burke, M. S. et al. Revised Oxygen Evolution Reaction Activity Trends for First-Row Transition-Metal (Oxy)hydroxides in Alkaline Media. *J. Phys. Chem. Lett.* **6**, 3737-3742 (2015).
3. Zou, S. et al. Fe (Oxy)hydroxide Oxygen Evolution Reaction Electrocatalysis: Intrinsic Activity and the Roles of Electrical Conductivity, Substrate, and Dissolution. *Chem. Mater.* **27**, 8011-8020 (2015).
4. Lim, J. et al. Ultrathin IrO_2 Nanoneedles for Electrochemical Water Oxidation. *Adv. Funct. Mater.* **28**, 1704796 (2018).
5. Xu, D. et al. Earth-Abundant Oxygen Electrocatalysts for Alkaline Anion-Exchange-Membrane Water Electrolysis: Effects of Catalyst Conductivity and Comparison with Performance in Three-Electrode Cells. *ACS Catal.* **9**, 7-15 (2019).
6. Yang, C. et al. Revealing pH-Dependent Activities and Surface Instabilities for Ni-Based Electrocatalysts during the Oxygen Evolution Reaction. *ACS Energy Lett.* **3**, 2884-2890 (2018).
7. McCrory, C. C. L., Jung, S., Peters, J. C. & Jaramillo, T. F. Benchmarking Heterogeneous Electrocatalysts for the Oxygen Evolution Reaction. *J. Am. Chem. Soc.* **135**, 16977-16987 (2013).
8. Filimonenkov, I. S. et al. Rotating Ring-disk Electrode as a Quantitative Tool for the Investigation of the Oxygen Evolution Reaction. *Electrochim. Acta* **286**, 304-312 (2018).
9. Corrigan, D. A. The Catalysis of the Oxygen Evolution Reaction by Iron Impurities in Thin Film Nickel Oxide Electrodes. *J. Electrochem. Soc.* **134**, 377-384 (1987).
10. Trotochaud, L., Young, S. L., Ranney, J. K. & Boettcher, S.W. Nickel Iron Oxyhydroxide Oxygen Evolution Electrocatalysts: The Role of Intentional and Incidental Iron Incorporation. *J. Am. Chem. Soc.* **136**, 6744-6753(2014).
11. Chakthranont, P. et al. Effects of Gold Substrates on the Intrinsic and Extrinsic Activity of High-Loading Nickel-Based Oxyhydroxide Oxygen Evolution Catalysts. *ACS Catal.* **7**, 5399-5409 (2017).
12. Klaus, S., Cai, Y., Louie, M. W., Trotochaud, L. & Bell, A. T. Effects of Fe Electrolyte Impurities on $Ni(OH)_2$/NiOOH Structure and Oxygen Evolution Activity. *J. Phys. Chem. C* **119**, 7243-7254 (2015).
13. Frydendal, R. et al. Enhancing Activity for the Oxygen Evolution Reaction: The Beneficial Interaction of Gold with Manganese and Cobalt Oxides. *ChemCatChem* **7**, 149-154 (2015).
14. Wei, J. Gold-supported cerium-doped NiOx catalysts for water oxidation. *Nat. Energy* **1**, 16053 (2016)
15. Chakthranont, P. et al. Effects of Gold Substrates on the Intrinsic and Extrinsic Activity of High-Loading Nickel-Based Oxyhydroxide Oxygen Evolution Catalysts. *ACS Catal.* **7**, 5399-5409 (2017).
16. Friebel, D. et al. Identification of Highly Active Fe Sites in (Ni,Fe)OOH for Electrocatalytic Water Splitting. *J. Am. Chem. Soc.* **137**, 1305-1313 (2015).
17. Minguzzi, A. et al. Observing the oxidation state turnover in heterogeneous iridium-based water oxidation catalysts. *Chem. Sci.* **5**, 3591-3597 (2014).
18. Bocquet, A.E. et al. Electronic structure of $SrFe^{4+}O_3$ and related Fe perovskite oxides. *Phys. Rev. B* **45**, 1561-1570 (1992).
19. Chen, J. Y. C. et al. Operando Analysis of NiFe and Fe Oxyhydroxide Electrocatalysts for Water Oxidation: Detection of Fe^{4+} by Mossbauer Spectroscopy. *J. Am. Chem. Soc.* **137**, 15090-15093 (2015).
20. Hunter, B. M. et al. Trapping an Iron (VI) Water-Splitting Intermediate in Nonaqueous Media. *Joule* **2**, 747-763 (2018).
21. Westre, T. E. et al. A multiplet Analysis of Fe K-Edge 1s → 3d Pre-Edge Features of Iron Complexes. *J. Am. Chem. Soc.* **119**, 6297-6314 (1997).
22. Song, F. et al. An Unconventional Iron Nickel Catalyst for the Oxygen Evolution Reaction. *ACS Cent. Sci.* **5**, 558-568 (2019).
23. Subbaraman, R. et al. Tr ends in activity for the water electrolyzer reactions on 3d M(Ni,Co,Fe,Mn) hydr(oxy)oxide catalysts. *Nat. Mater.* **11**, 550-557 (2012).

24. Danilovic, N. et al. Enhancing the alkaline hydrogen evolution reaction activity through the bifunctionality of $Ni(OH)_2$/metal catalysts. *Angew. Chem. Int. Ed.* **124**, 12663-12666 (2012).
25. Strmcnik, D., Lopes, P. P., Genorio, B., Stamenkovic, V. R. & Markovic, N. M. Design principles for hydrogen evolution reaction catalyst materials. *Nano Energy* **29**, 29-36 (2016).